



# Fast anisotropic Mg and H diffusion in wet forsterite

Joshua M. R. Muir<sup>1,3</sup> · Feiwu Zhang<sup>1</sup> · Andrew M. Walker<sup>2,3</sup>

Received: 2 January 2022 / Accepted: 28 May 2022 / Published online: 25 July 2022  
© The Author(s), under exclusive licence to Springer-Verlag GmbH Germany, part of Springer Nature 2022

## Abstract

Adding hydrogen to forsterite strongly increases the diffusion rate of Mg, but the reason for this is unclear. As Mg diffusion in forsterite can influence its electrical conductivity, understanding this process is important. In this study we use density functional theory to predict the diffusivity of H-bearing Mg vacancies and we find that they are around 1000 times slower than H-free Mg vacancies. H-bearing Mg vacancies are many orders of magnitude more concentrated than H-free Mg vacancies, however, and diffusion is a combination of diffusivity and defect concentration. Overall, the presence of hydrated Mg vacancies is predicted to cause a large (multiple orders of magnitude) increase in both diffusion rate and diffusional anisotropy with a strong preference for diffusion in the [001] direction predicted. In models of experimental data, the effect of water concentration on diffusion is often described by a constant best-fitting exponent. Our results suggest that this exponent will vary between 0.5 and 1.6 across common experimental conditions with pressure decreasing and temperature increasing this exponent. These results suggest that Mg diffusion in forsterite could vary considerably throughout upper mantle conditions in ways that cannot be captured with a simple single-exponent model. Comparisons to measures of hydrogen diffusivity suggest that the diffusion of hydrated Mg vacancies also controls the diffusion of hydrogen in (iron-free) forsterite and that our conclusions above also apply to hydrogen diffusion rates and anisotropy. We also find that cation diffusivity likely cannot explain experimental measurements of the effect of water on electrical conductivity in olivine.

## Plain Language Summary

Olivine is an important component of the upper mantle and its properties largely control the properties of the upper mantle. These properties can be strongly affected by the presence of water even in small quantities. In this work we look at the effect of water on one such property—the diffusion of Mg atoms. We find that water can increase both the rate of diffusion and the directional preference of this diffusion by multiple orders of magnitude. Importantly the effect of water is highly dependent upon the prevailing conditions such as pressure, temperature, the buffer for silica activity and the presence or absence of Ti. This means that the effect of water on this property can vary throughout mantle conditions. Our results are also found to apply to the diffusion of hydrogen in forsterite which appears to diffuse through the same mechanism. We also used a simple model of olivine conductivity to predict the effect of water on conductivity. Water has previously been measured to increase conductivity in olivine but our model fails to replicate this effect in multiple ways. This suggests the conductivity increase induced by water in olivine is not due to an increase in ionic diffusion but is due to another unknown mechanism.

**Keywords** Forsterite · Mg Diffusion · Water · Hydrogen · DFT

---

✉ Joshua M. R. Muir  
j.m.r.muir@mail.gyig.ac.cn

Feiwu Zhang  
zhangfeiwu@vip.gyig.ac.cn

<sup>1</sup> State Key Laboratory of Ore Deposit Geochemistry, Institute of Geochemistry, Chinese Academy of Sciences, 99 West Lincheng Road, Guiyang 550081, Guizhou, China

<sup>2</sup> Department of Earth Sciences, University of Oxford, South Parks Road, Oxford OX1 3AN, UK

<sup>3</sup> Department of Earth Sciences, University of Leeds, Leeds LS2 9JT, UK

## Introduction

Diffusion of Mg in olivine is an important control on electrical conductivity (Fei et al. 2018; Yoshino et al. 2009, 2017; Schock et al. 1989; Sun et al. 2019; Gardes et al. 2014) in the upper mantle and potentially on deformation (Jaoul 1990), grain growth (Jung and Karato 2001) and texture development (Karato et al. 2008). For this reason, Mg diffusion rates have been studied extensively (see for example discussions in Charkaborty 2010 and Jollands et al. 2020).

An important control on this diffusion rate in the upper mantle will be water (Demouchy and Bolfan-Casanova 2016). Adding a small amount of water (~ 100 ppm) in the form of OH<sup>-</sup> groups incorporated within the olivine crystal has been found to significantly enhance Mg diffusion rates (Fei et al. 2018) at 1300 K and 8 GPa. Hydrous diffusion has been described with the equation:  $D_{Mg} = D_0(C_{H_2O})^r \exp(-\frac{H_m}{RT})$ .  $D_0$  and  $H_m$  are fitting variables (the diffusion coefficient and activation enthalpy, respectively) and  $CH_2O$  is the concentration of water in the sample. The effect of water is described by the exponent  $r$  which has been found to be  $1.2 \pm 0.2$  for Mg tracer diffusion (Fei et al. 2018) and to be ~ 1 for Fe–Mg interdiffusion (Wang et al. 2004). However, this water exponent is difficult to constrain by experiment as diffusion increases with water content but decreases with pressure, which also increases water fugacity. The mechanism by which water changes the diffusion rate is still unclear and experimental data points are limited.

Thus in this work, we use atomic-scale simulation with Density Functional Theory (DFT) to examine a possible mechanism by which water affects Mg diffusion, the production and diffusion of H-bearing Mg vacancies, and then calculate how varying conditions across pressure, temperature and composition space would affect this mechanism. The effect of condition and composition space is important for extrapolation across the varied conditions in the upper mantle and to enable comparison between experiments.

## Methods

Diffusion is very slow compared to the timescales of atomistic simulations. To account for this we use a hybrid Kinetic Monte Carlo (KMC) approach which is outlined in detail in Muir et al. (2021) and in the supplementary method. In short, we first define the diffusing species ( $V''_{Mg}$ ,  $Mg_I^{**}$ ,  $(2H)_{Mg}^X$  all listed with Kröger-Vink notation (Kroger and Vink 1956)) and determine their structure and position in the forsterite lattice using Density Functional Theory (DFT) as outlined in the supplementary method. We then determined their high-temperature energy using lattice dynamics and the quasi-harmonic approximation (QHA) and the energy of

alternative defects into which they can transform to build a thermodynamic model of defect concentrations with which we calculate the concentration of each defect. The method for this is outlined in full in Muir et al. (2022) with some more details in the supplementary information. Second we determine all the possible “hops” between the different neighbouring positions the defects can occupy and probe the energy landscape along with these hops. This provides an energy barrier that each hop must overcome and the frequency at which this hop is attempted. Third, we combine information about multiple hops between different ground states using a kinetic Monte Carlo approach to access time-scales long enough to observe the random walk and measure Mg diffusion in forsterite using the method described in Muir et al. (2021) and the supplementary information.

## Diffusion hops

To calculate diffusion coefficients we extend the method in Muir et al. (2021) to include H-bearing Mg vacancies alongside consideration of anhydrous defects. For each considered defect  $V''_{Mg}$ ,  $Mg_I^{**}$ ,  $(2H)_{Mg}^X$  we define movement as a series of hops between different Mg sites (M1 and M2). We have assumed the simplest possible hopping mechanism and one that does not involve multi-atom hops. We have assumed that the concentration of defects is low enough that defect–defect effects do not affect hopping. We used all possible hops from an Mg site to nearest and next-nearest neighbours that did not cross any other atoms and these are listed in Table 1 though we have excluded any multi-atom or long-range hops. For each hop, we calculate the activation enthalpy by constructing a pathway along the hop and moving an Mg atom along this pathway. At each point the Mg atom is constrained to the path and the highest energy of the path (the transition state) is found. Once the transition state is determined we calculate its phonon frequencies using lattice dynamics and find the attempt frequency of the hop using Vineyard theory (Vineyard 1957) as described in Muir et al. (2021). The rate of each hop is then determined with:

$$k = v^* \exp\left(-\frac{H_m}{k_B T}\right) \quad (1)$$

where  $v^*$  is the attempt frequency from Vineyard theory and  $H_m$  is the activation enthalpy. All the possible hop rates are then entered into our KMC model which is outlined in the supplementary method and in Muir et al. (2021) and a diffusion coefficient determined. This model operates by first determining the relative probability of each hop (from the activation enthalpy and attempt frequencies) and by then drawing a weighted random number so that a hop is chosen. Once a hop is chosen the diffusing atom is moved through space along one-hop distance. Using the hopping rates and

**Table 1** List of different  $(2H)_{Mg}^X$  hops and the absolute hop distance of the centre of the vacancy in unit cell values (at 0 GPa uncorrected these are 4.80, 10.32 and 6.04 Å respectively) and their degeneracy

Site	[100]	[010]	[001]	Degeneracy	Hops between sites starting from 1/5	Possible directions from sites 1/5	Sample probability (1500 K, 5 GPa)
Vacancy hops from M1							
A	0.000	0.000	0.500	2	1–3	+ c, – c	0.64
B	1.000	0.000	0.000	2	1–1	+ a, – a	0.00
C	0.009	0.277	0.250	2	1–6/7	– a + b + c, + a – b – c	0.16
D	0.491	0.223	0.250	2	1–5/8	– a – b + c, + a + b – c	0.00
D*	0.509	0.223	0.250	2	1–5/8	+ a – b + c, – a + b – c	0.00
Vacancy hops from M2 site							
C	0.009	0.277	0.250	2	5–2/4	– a – b – c, – a – b + c	0.02
D	0.491	0.223	0.250	2	5–1/3	+ a + b – c, + a + b + c	0.09
D*	0.509	0.223	0.250	2	5–1/3	– a + b – c, – a + b + c	0.08
E	0.500	0.055	0.500	4	5–7	+ a – b + c, + a – b – c, – a – b + c, – a – b – c	0.01
F	1.000	0.000	0.000	2	5–5	+ a, – a	0.00

To illustrate the degeneracy of the hops we have shown the possible hops between different sites and the different degenerate directions with hops starting from site 1 (an M1 site, M1 sites are 1–4) and from site 5 (an M2 site, M2 sites are 5–8). The final column indicates the probability that any random hop will be of the type listed determined from a 1500 K, 5 GPa run

a second weighted random number a hopping time can be chosen and the atom is also moved forward through time. By repeating this process millions of times the atom randomly diffuses through space and time and a diffusion coefficient can be determined through its mean-squared displacement against time. Diffusion coefficients were calculated at 0, 5, 10 and 15 GPa (uncorrected) and at 1000, 1500 and 2000 K.

The hops and diffusion coefficients for the two anhydrous Mg defects— $V''_{Mg}$  and  $Mg_I^*$ —are shown in Muir et al. (2021). In this work, we also consider the diffusion of  $(2H)_{Mg}^X$ . The centre of the  $(2H)_{Mg}^X$  vacancy undergoes the same lattice hops (under the assumption of single site hops to neighbours) with the same labelling as in  $V''_{Mg}$  which are described in Muir et al. (2021) and are listed in Table 1. This method constrains  $(2H)_{Mg}^X$  to an Mg lattice site and then allows it to hop between every nearest and next nearest Mg lattice site in every possible direction.

The hops of  $(2H)_{Mg}^X$  are more complex than those of  $V''_{Mg}$ , however, due to the presence of the hydrogen atoms. When determining the energy of the transition state for hydrous vacancies we assumed that hydrogen mobility is much higher than magnesium mobility (Novella et al. 2017) and so the hydrogen atoms follow the vacancy adiabatically. The procedure followed for hydrous vacancies is that described above (moving a Mg atom along the pathway and constrained to the pathway) but with hydrogen placed in a range of different positions (and relaxed without constraints) for each image. Hydrogen ions were placed in the  $MO_6$  octahedron at the start or end of the path leading to four

configurations for each image. One of these has two hydrogen atoms in the “start” octahedron, one has two hydrogen atoms in the “end” octahedron and two configurations have one hydrogen in each octahedron. Each point of the path then has four energies and at each point, the lowest energy is selected to construct the path and find the transition state. In all cases, the hopping Mg atom was fixed to the path and all other atoms were allowed to relax including hydrogen. When relaxing the hydrogen atoms they will only find the local minimum from their starting point necessitating multiple starting points for hydrogen positions. In each step, the enthalpy of binding H to each O in the vacancy was calculated and the lowest used. All transition states determined by this method had exactly 1 imaginary frequency in the phonon spectrum (confirming that they are indeed transition states) and all starting/ending states had 0 imaginary frequencies. A sample minimum energy path is shown in Fig. S1 and a sample transition state in Fig. S2. This procedure assumes that throughout the process of magnesium diffusion the hydrogen atoms can rearrange to minimise the energy. We also attempted placing H outside the two  $MO_6$  octahedra, but this always gave higher energies than the previous configurations. In this way, our activation enthalpies for diffusion in hydrous forsterite are the minimum possible barriers as they ignore any barriers to hydrogen migration. Unless the energy of these hydrogen mobility barriers is close to the barriers of Mg migration they will be unimportant to the final rate of diffusion as diffusion rates are generally controlled by the rate of their slowest step. We ignore the dynamics of hydrogen motion and for each Mg displacement

along the pathway we only consider the lowest enthalpy of all tested hydrogen arrangements and ignore the enthalpy of all other hydrogen arrangements.

## Diffusion

Diffusion is then calculated with:

$$D_{Mg}^{sd} = D_{Mg}^{Vac} N_{Vac} + D_{Mg}^{Int} N_{Int} + D_{Mg}^{HVac} N_{HVac} \quad (2)$$

where  $D_{Mg}^{HVac}$  is the self-diffusion coefficient for  $(2H)_{Mg}^X$  as determined from the KMC model and  $N_{HVac}$  is the concentration of  $(2H)_{Mg}^X$  and the same for interstitials and Mg vacancies. We consider Mg diffusion to be independent of Si and O diffusion (i.e., the interdiffusion coefficients are 0). In anhydrous forsterite the concentrations of  $V_{Mg}''$  and  $Mg_I^{**}$  can be reliably approximated using only the thermodynamic equilibrium of the Frenkel reaction (Muir et al. 2021). Determining the concentration of defects in hydrous forsterite is much more difficult because there are multiple viable H-bearing defects that can form (such as  $(2H)_{Mg}^X$ ,  $(4H)_{Si}^X$ , and in the presence of Ti  $Ti_{Mg}^{**}$ ,  $(2H)_{Si}''$ ) and the presence of these defects also affects the concentration of the H-free and intrinsically formed defects. To account for this we built a thermodynamic model of point defect concentrations in forsterite, described in detail in Muir et al. (2022) with some more information in the supplementary information. In essence, this model takes the energy of a variety of defect-producing (such as the Mg Frenkel reaction) and transforming (such as a reaction turning  $(2H)_{Mg}^X$  into  $(4H)_{Si}^X$ ) reactions using DFT and QHA at a variety of pressures and temperatures. At the desired pressure, temperature and composition we then solve for the concentration and distribution of defects that gives the minimum free energy. The model is built for pure forsterite and for forsterite containing Ti, Al and H. In this work, we take the concentrations of defects produced by the thermodynamic model at appropriate temperatures, pressures and compositions and feed these into Eq. 2.

The four main sources of error in our diffusion model are (1) statistical error from our KMC model, (2) errors in attempt frequency, activation enthalpies and defect energies from using finite energy cutoffs and limited k and q-points in DFT- notably we calculate phonon frequencies at a single q-point (3) systematic error of DFT in determining attempt frequencies, activation enthalpies and defect energies and (4) the effect of any real physical mechanisms which are not present in our model. The first two sets of error can be bounded by tests and our attempts to do so are listed in the supplementary information. Notably doubling the sampling time of our KMC model changed the calculated diffusivities by less than 0.01% (the first type of errors are likely small) and increasing the q-points of one of our hops

changed diffusivities by < 0.7%. Assigning error from the first two sources potentially underestimates the error on diffusion rates from our model as the undefined error from the latter two sources maybe important. Thus determining the validity of our diffusion rates can only be reliably performed by comparisons with experimental data. As seen in the text we can replicate some experimental data points (Figs. 2 and 4) suggesting the effects of all of these sources are error are not large.

While the errors in the absolute rates are not determined the errors in relative rates of diffusion as pressure, temperature and water concentration vary should be much smaller. In these cases, a lot of the absolute errors of DFT calculations cancel out and the variation in diffusion rates are largely controlled by reliable thermodynamic equations such as the Arrhenius equation of Eq. 1 or the configurational entropy equations which control the variations of H-bearing defects (Muir et al. 2022). Thus our predictions in trends of diffusion rates (such as in Table 5 fitting to Eq. 4) with varying conditions are expected to be more reliable than absolute diffusion rates.

## Pressure correction

While DFT generally reliably reproduces pressure derivatives, the absolute pressures calculated by DFT are known to be systematically incorrect in that they are shifted in one direction. To correct for these we used a simple linear correction

$$P(V, T) = P^{DFT}(V, T) - P^{DFT}(V_0^{exp}) \quad (3)$$

where the subscript 0 represents the value of a parameter at a reference volume. For this equation we used  $V_0^{exp}$  values of 287.4 Å<sup>3</sup> for olivine (Isaak et al. 1989), 74.71 Å<sup>3</sup> for MgO (Speziale et al. 2001) and 832.918 Å<sup>3</sup> for enstatite (Kung et al. 2004). This provided corrections of − 4.95, − 4.45 and − 3.91 GPa respectively. The energy of our reactions was then adjusted to account for these different pressure corrections using our calculated dE/dP values as were the diffusion coefficients. All pressures are presented corrected unless stated.

## Units

Water in this paper shall refer to H-bearing defects. Concentrations shall be given as  $[H_2O]_{bulk}$ . This is the sum of the concentrations of all H-bearing defects with the concentrations of each defect normalised to contain the same amount of hydrogen as water. These are given in wt. ppm (1 wt. ppm = 15.6 H/Si 10<sup>6</sup>). Concentrations of Ti are given as wt. ppm TiO<sub>2</sub>. “Pure” forsterite in this paper refers to forsterite

**Table 2** Activation enthalpies (in eV) and modified attempt frequency  $v^*$  (in log Hz) as a function of uncorrected pressure for different hops for  $(2H)_{Mg}^X$

		0 GPa		5 GPa		10 GPa		15 GPa	
		$H_m$ (eV)	$v^*$ (log Hz)	$H_m$ (eV)	$v^*$ (log Hz)	$H_m$ (eV)	$v^*$ (log Hz)	$H_m$ (eV)	$v^*$ (log Hz)
Hops from M1 site									
A	M1-M1	1.26	12.74	1.23	12.99	1.20	13.07	1.17	13.12
B	M1-M1	3.81	14.45	4.21	14.34	4.53	14.33	4.83	14.35
C	M1-M2	1.41	13.70	1.64	13.78	1.82	13.94	1.99	14.07
D	M1-M2	2.20	14.03	2.47	14.19	2.68	14.36	2.88	14.49
D*	M1-M2	2.20	14.03	2.47	14.19	2.68	14.36	2.88	14.49
Hops from M2 site									
C	M2-M1	0.76	12.65	0.85	13.57	0.96	13.88	1.07	14.06
D	M2-M1	1.55	12.97	1.68	13.98	1.82	14.30	1.96	14.49
D*	M2-M1	1.55	12.97	1.68	13.98	1.82	14.30	2.55	14.49
E	M2-M2	1.87	13.27	2.08	13.93	2.31	14.58	2.55	14.85
F	M2-M2	2.80	12.86	3.18	13.20	3.46	13.47	3.72	13.64

with no other defects (such as Ti) except H-bearing defects in the presence of water.

## Results

### Diffusion coefficients of hydrous defects

Table 2 presents the activation enthalpy and attempt frequency of various hops of  $(2H)_{Mg}^X$ . Two hops have the lowest activation enthalpies, the “A” and the “C” hop. The other hops are far less important and these two hops largely control diffusion. The “A” hop is between two M1 sites along the [001] direction whereas the “C” hop is between an M1 and a M2 site along primarily the [011] direction. This means that  $(2H)_{Mg}^X$  on an M1 site primarily diffuses along [001] while remaining in M1 sites and that any  $(2H)_{Mg}^X$  that escapes to an M2 site will quickly convert back to an M1 site through a “C” hop. This behaviour is extremely similar to that of  $V_{Mg}''$  as outlined in Muir et al. (2021). Every other hop in every other direction is unfavourable enough that excluding them makes a negligible difference to the calculated diffusivities. The prominence of the “A” hop and thus the predicted anisotropy of diffusion (see below) is unsurprising when the forsterite crystal structure is considered as there are chains of M1 sites in the [001] direction with no intervening atoms to retard diffusion whereas all other directions in the crystal contain atomistic barriers which must be overcome to diffuse in that direction.

Our calculated diffusion coefficients of  $V_{Mg}''$ ,  $Mg_I^{**}$  and  $(2H)_{Mg}^X$  are presented in Table 3. Discussion of the diffusivity of  $V_{Mg}''$  and  $Mg_I^{**}$  and more values are given in Muir et al. (2021). We find that  $(2H)_{Mg}^X$  has diffusivities that are around 1–3 orders of magnitude slower than those of  $V_{Mg}''$  with the difference decreasing with increasing temperature. In both

cases diffusion is predominantly controlled by the “A” hop. For  $V_{Mg}''$  the activation enthalpy of this hop is 0.75 eV (Muir et al. 2021) but for  $(2H)_{Mg}^X$  it is around 1.2–1.3 eV (Table 2) which largely accounts for the slower diffusivity of  $(2H)_{Mg}^X$ . This increase in the activation enthalpy of  $(2H)_{Mg}^X$  hopping is due to the presence of H atoms which increase repulsion for a moving Mg atom. The predominance of the “A” hop leads  $V_{Mg}''$  and  $(2H)_{Mg}^X$  to diffuse in a highly anisotropic manner with diffusion along the [001] direction being orders of magnitude faster than diffusion along the [010] or [100] directions. This anisotropy is much larger at lower temperatures because diffusion rates depend upon an exponential function of temperature ( $e^{-\frac{E_a}{k_b T}}$ ). Increasing the pressure increases this anisotropy but to a much smaller degree than lowering temperature.

### Diffusion rates

To solve Eq. 2 we need the diffusivities of various species (Sect. 3.1) and their concentration. In Muir et al. (2022) we predicted that the main sites for water in forsterite are  $(2H)_{Mg}^X$ ,  $(4H)_{Si}^X$  and, if Ti is present,  $\{Ti_{Mg}^{**}(2H)_{Si}''\}^X$ . Of these we shall focus on the diffusion of  $(2H)_{Mg}^X$  as we do not expect the other defects to contribute significantly to Mg diffusion.  $(4H)_{Si}^X$  has no straightforward effect on Mg diffusion as it exists on a Si site and  $\{Ti_{Mg}^{**}(2H)_{Si}''\}^X$  is likely immobile based on experimental measurements of hydrogen diffusion rates in Ti-bearing forsterite (Jollands et al. 2016). Our calculations also suggest that  $\{Ti_{Mg}^{**}(2H)_{Si}''\}^X$  is immobile because we calculate the binding energy of the two components to be very high (~ 5–6 eV across upper mantle conditions depending upon pressure and temperature). To diffuse  $\{Ti_{Mg}^{**}(2H)_{Si}''\}^X$  it would either have to overcome this barrier which is much higher than the diffusion barriers of  $(2H)_{Mg}^X$



**Table 3** Calculated diffusivity coefficients (in  $m^2s^{-1}$ ) for  $Mg_{S_{Mg}}^{**}$ ,  $Vac_{Mg}''$  and  $(2H)_{Mg}^X$  as a function of corrected pressure and temperature

		$D_{Mg}^{int}$			$D_{Mg}^{vac}$			$D_{Mg}^{H_{Mg}^X}$		
		[100]	[010]	[001]	[100]	[010]	[001]	[100]	[010]	[001]
0 GPa	1000 K	$2.94 \times 10^{-12}$	$1.16 \times 10^{-11}$	$6.13 \times 10^{-12}$	$3.92 \times 10^{-14}$	$1.64 \times 10^{-13}$	$1.88 \times 10^{-10}$	$4.70 \times 10^{-17}$	$6.49 \times 10^{-17}$	$5.17 \times 10^{-13}$
	1500 K	$1.23 \times 10^{-11}$	$4.45 \times 10^{-11}$	$2.07 \times 10^{-11}$	$1.89 \times 10^{-10}$	$4.99 \times 10^{-10}$	$3.63 \times 10^{-9}$	$1.34 \times 10^{-13}$	$1.12 \times 10^{-12}$	$1.24 \times 10^{-10}$
	2000 K	$3.09 \times 10^{-11}$	$1.06 \times 10^{-10}$	$4.37 \times 10^{-11}$	$1.24 \times 10^{-9}$	$3.24 \times 10^{-9}$	$1.52 \times 10^{-8}$	$8.70 \times 10^{-13}$	$7.49 \times 10^{-12}$	$7.19 \times 10^{-10}$
5 GPa	1000 K	$2.04 \times 10^{-11}$	$9.05 \times 10^{-11}$	$6.66 \times 10^{-11}$	$7.95 \times 10^{-14}$	$2.11 \times 10^{-13}$	$1.88 \times 10^{-10}$	$4.94 \times 10^{-18}$	$6.10 \times 10^{-18}$	$6.97 \times 10^{-13}$
	1500 K	$5.06 \times 10^{-11}$	$1.94 \times 10^{-10}$	$9.55 \times 10^{-11}$	$2.80 \times 10^{-10}$	$6.16 \times 10^{-10}$	$3.38 \times 10^{-9}$	$2.34 \times 10^{-14}$	$2.02 \times 10^{-13}$	$1.57 \times 10^{-10}$
	2000 K	$9.74 \times 10^{-11}$	$3.26 \times 10^{-10}$	$1.20 \times 10^{-10}$	$1.81 \times 10^{-9}$	$3.96 \times 10^{-9}$	$1.42 \times 10^{-8}$	$1.54 \times 10^{-13}$	$1.36 \times 10^{-12}$	$9.08 \times 10^{-10}$
10 GPa	1000 K	$1.16 \times 10^{-10}$	$3.60 \times 10^{-10}$	$3.40 \times 10^{-10}$	$1.27 \times 10^{-13}$	$1.65 \times 10^{-13}$	$1.87 \times 10^{-10}$	$3.03 \times 10^{-19}$	$1.06 \times 10^{-18}$	$1.13 \times 10^{-12}$
	1500 K	$1.18 \times 10^{-10}$	$4.52 \times 10^{-10}$	$2.27 \times 10^{-10}$	$1.72 \times 10^{-10}$	$4.35 \times 10^{-10}$	$3.20 \times 10^{-9}$	$1.09 \times 10^{-14}$	$6.60 \times 10^{-14}$	$1.73 \times 10^{-10}$
	2000 K	$2.08 \times 10^{-10}$	$6.74 \times 10^{-10}$	$2.41 \times 10^{-10}$	$1.06 \times 10^{-9}$	$2.73 \times 10^{-9}$	$1.28 \times 10^{-8}$	$7.38 \times 10^{-14}$	$4.52 \times 10^{-13}$	$9.08 \times 10^{-10}$

or it would have to undergo some multipart diffusion. Multipart diffusion is likely also be slow as it would involve overcoming multiple barriers that are likely higher than those of  $(2H)_{Mg}^X$  as they would involve moving atoms through spaces more congested than the [001] M1 chains. Thus the important factor in wet Mg diffusion is  $[(2H)_{Mg}^X]$ .

Our predicted concentrations of defects are listed in Table 4. As was found in Muir et al. (2022)  $(2H)_{Mg}^X$  is favoured at high temperatures, low pressures and low water concentrations and thus Mg diffusion will be faster at these conditions. Free interstitial  $H_i^+$  is relatively favoured by low water concentrations and higher temperatures but its concentration is always predicted to be extremely low.  $[Mg_I^{**}]$  is suppressed by the addition of more water while  $[V_{Mg}^{**}]$  can both increase and decrease with the addition of water. In all cases, H-bearing defects are predicted to greatly outnumber H-free defects.

Our predicted diffusion rates as a function of water are shown for pure forsterite in Fig. 1 and in the presence of Ti alongside experimental data (Fei et al. (2018)) in Fig. 2. In general, there is initially a very sharp increase in diffusion rate with increasing amounts of water- conversion from a “dry” to a “wet” regime- and then a slower increase in diffusion with increasing water- the “wet” regime. In the “dry” regime  $[V_{Mg}^{**}]$  is much larger than  $[(2H)_{Mg}^X]$  or they have similar values. In the “wet” regime  $[(2H)_{Mg}^X]$  is much larger than  $[V_{Mg}^{**}]$ .

For the comparisons to the values of Fei et al. (2018) in Fig. 2 we present both “pure” forsterite and forsterite with 80 wt. ppm  $TiO_2$ , as  $TiO_2$  is one of the impurities present in the experiments of Fei et al. (2018) and it is one which could affect wet diffusion by allowing the formation of immobile  $\{Ti_{Mg}^{**}(2H)_{Si}''\}^X$ . We find that Ti can cause a difference in diffusion rates at low pressures, low temperatures and low water concentrations through the formation of  $\{Ti_{Mg}^{**}(2H)_{Si}''\}^X$  over  $(2H)_{Mg}^X$  but that at the conditions used in Fei et al. (2018) Ti-free and Ti-containing samples largely have identical traces because  $(4H)_{Si}^X$  is favoured over both  $\{Ti_{Mg}^{**}(2H)_{Si}''\}^X$  and  $(2H)_{Mg}^X$ .

We fit an equation to plot the effect of water on the diffusion rate:

$$D_{sd} = a + [H_2O]_{bulk}^r * b \tag{4}$$

where  $a$ ,  $b$  and  $r$  are fitting variables. Such equations are commonly used to fit the effects of water to diffusion (see for example (Fei et al. 2018)) and so the ability or inability to obtain a good fit to such an equation matters. The results are shown in Table 5 (anisotropy and Ti-free values) and Table 6 (Ti-bearing values). We did this separately for the “dry” and the “wet” regime. The  $[H_2O]_{bulk}$  value at which the “wet” region begins is tabulated in Table 5 and for “pure” forsterite

**Table 4** Log of the concentration (in defects/f.u.) of major defects in a system of “pure forsterite” predicted at different temperatures, corrected pressures and water concentrations

		1000 K			1500 K			2000 K		
		0 GPa	5 GPa	10 GPa	0 GPa	5 GPa	10 GPa	0 GPa	5 GPa	10 GPa
[H <sub>2</sub> O] <sub>bulk</sub> 1 wt.ppm	[(4H) <sub>Si</sub> <sup>X</sup> ]	-5.46	-5.41	-5.41	-6.46	-5.50	-5.41	-8.02	-6.78	-5.43
	[(2H) <sub>Mg</sub> <sup>X</sup> ]	-6.09	-7.65	-10.82	-5.15	-5.85	-8.46	-5.11	-5.13	-6.52
	[H <sub>i</sub> <sup>+</sup> ]	-15.94	-15.24	-15.09	-11.51	-14.72	-14.73	-9.00	-12.10	-14.47
	[V <sub>Mg</sub> <sup>''</sup> ]	-15.90	-15.45	-15.32	-11.80	-14.56	-14.57	-8.24	-9.70	-10.35
	[Mg <sub>T</sub> <sup>**</sup> ]	-16.16	-16.16	-16.16	-13.93	-14.56	-14.79	-8.28	-9.70	-10.35
[H <sub>2</sub> O] <sub>bulk</sub> 10 wt.ppm	[(4H) <sub>Si</sub> <sup>X</sup> ]	-4.42	-4.41	-4.41	-4.81	-4.44	-4.41	-6.04	-5.00	-4.41
	[(2H) <sub>Mg</sub> <sup>X</sup> ]	-5.58	-7.15	-10.31	-4.32	-5.32	-7.96	-4.12	-4.24	-6.02
	[H <sub>i</sub> <sup>+</sup> ]	-14.90	-14.99	-15.04	-11.52	-14.68	-14.68	-9.00	-12.10	-14.38
	[V <sub>Mg</sub> <sup>''</sup> ]	-15.16	-15.23	-15.45	-11.81	-14.73	-14.63	-8.98	-10.58	-10.85
	[Mg <sub>T</sub> <sup>**</sup> ]	-16.16	-16.16	-16.16	-14.41	-14.74	-14.73	-9.27	-10.58	-10.85
[H <sub>2</sub> O] <sub>bulk</sub> 100 wt.ppm	[(4H) <sub>Si</sub> <sup>X</sup> ]	-3.41	-4.41	-3.41	-3.54	-3.42	-3.41	-4.18	-3.61	-3.41
	[(2H) <sub>Mg</sub> <sup>X</sup> ]	-5.07	-10.32	-9.80	-3.69	-4.81	-7.46	-3.19	-3.54	-5.52
	[H <sub>i</sub> <sup>+</sup> ]	-13.96	-14.89	-14.98	-11.53	-14.63	-14.63	-9.01	-12.10	-14.30
	[V <sub>Mg</sub> <sup>''</sup> ]	-14.25	-15.15	-15.23	-11.83	-14.81	-14.66	-9.26	-11.26	-11.37
	[Mg <sub>T</sub> <sup>**</sup> ]	-16.30	-16.16	-16.16	-14.51	-14.84	-14.69	-10.20	-11.27	-11.37

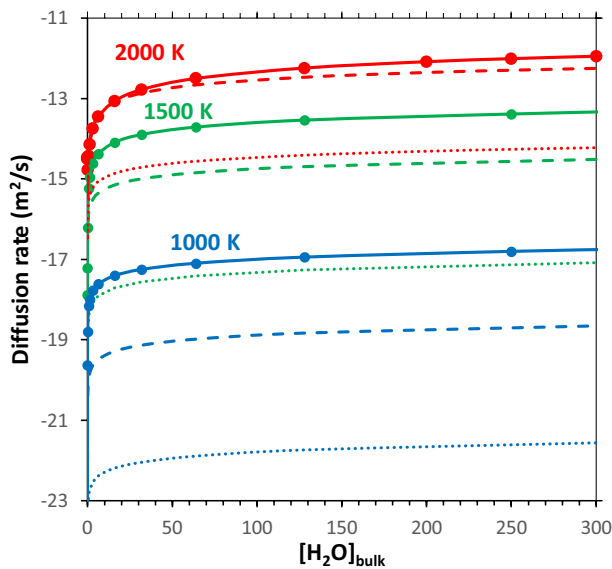


**Fig. 1** Predicted diffusion rates in pure forsterite as a function of [H<sub>2</sub>O]<sub>bulk</sub> at three different temperatures (2000 K=red, 1500 K=green, 1000 K=blue) and with three different corrected pressures (0 GPa=solid lines, 5 GPa=dashed line, 10 GPa=dotted lines). The same graph with a log scale of water is presented in Fig. S1. To create this graph diffusion was calculated at [H<sub>2</sub>O]<sub>bulk</sub> values of 0, 0.0064, 0.064, 0.64, 1.28, 3.20, 6.40, 16, 32.01, 64.02, 128, 200, 250, 300, 320.11 and 500 and then points were connected in a line. Individual diffusion points are shown for the 0 GPa samples but it is important to remember for this and all future plots that these points are not independent measurements and all derive from the same model and thus are highly correlated. All measurements fit near exactly into the plotted trends because of this correlation

is always below 1 wt. ppm. Thus at realistic concentrations of water only the “wet” region is important for Mg diffusion and these are the values presented in Table 5.

First, we shall consider the value of *r* which is the key variable in how changing the concentration of water changes diffusion rates. *r* varies strongly with conditions going from 0.55 at high pressure and low temperature to 0.88 at high temperature and low temperature in “pure” forsterite. In general increasing pressure decreases *r* and increasing temperature increases *r*. In the presence of Ti (Table 6) *r* has even more possible variations with increasing Ti leading to large increases in *r* particularly at low temperatures. Thus *r* is highly dependent upon experimental conditions and no one fitting of Eq. 4 or similar equations can capture the effect of water on Mg diffusion rates across mantle-relevant temperatures, pressures and compositions.

To understand why *r* varies with the condition we must consider how varying [H<sub>2</sub>O]<sub>bulk</sub> varies the diffusion rate. In the wet region where [(2H)<sub>Mg</sub><sup>X</sup>] >> [V<sub>Mg</sub><sup>''</sup>] the diffusion rate increases with increasing [H<sub>2</sub>O]<sub>bulk</sub> overwhelmingly because [(2H)<sub>Mg</sub><sup>X</sup>] increases. The rate of increase of the Mg diffusion rate is thus proportional to how [(2H)<sub>Mg</sub><sup>X</sup>] varies with [H<sub>2</sub>O]<sub>bulk</sub>:

$$[(2H)_{Mg}^X] \propto [H_2O]_{bulk}^{rc} \tag{5}$$

with the parameter *rc* in Eq. 5 taking a similar numerical value to *r* in Eq. 4. The variation of *rc* values with the condition is explored in detail in Muir et al. (2022) but in short *rc*

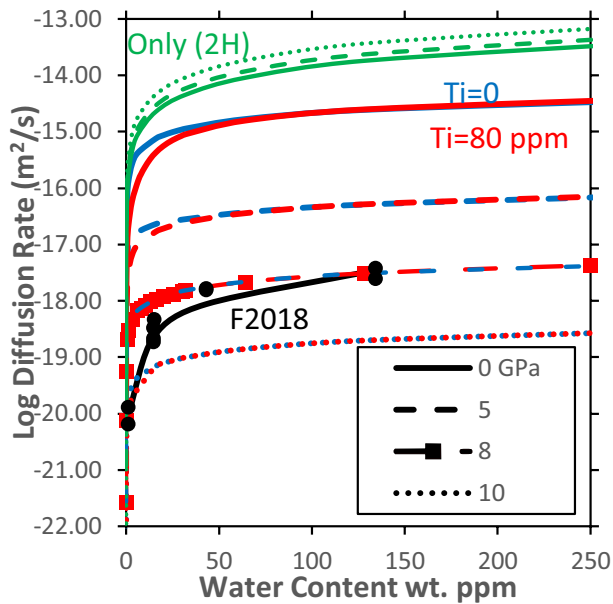


**Fig. 2** Plot of diffusion rate as a function of water content at 1300 K and at different corrected pressures. Three different sets of data are presented, green where all water is artificially  $(2H)_{Mg}^X$ , blue where the system is solved with no Ti ( $(2H)_{Mg}^X$  and  $(4H)_{Si}^X$ ) and red where the system is solved with  $TiO_2=80$  wt. ppm ( $(2H)_{Mg}^X$ ,  $(4H)_{Si}^X$  and  $\{Ti_{Mg}^{2+}(2H)_{Si}''\}$ ). The concentration of Ti was chosen to match that of Fei et al. (2018) whose results are presented in black and which were measured at  $\sim 1300$  K and 8 GPa. The  $Ti=0$  ppm and  $Ti=80$  ppm traces are similar at high water concentrations but diverge at lower water concentrations. The same plot with water plotted on a log scale is presented in Fig. S2. To construct this graph diffusion rates were calculated at  $[H_2O]_{bulk}$  values of 0.0064, 0.064, 0.64, 1.28, 3.20, 6.4, 8, 10, 13, 16.00, 20, 25, 30, 32, 64, 128, 250 and 320.1 wt. ppm and then a line plotted through these points. These points have been visualised for the 8 GPa, Ti containing run

values are heavily dependent on which H-bearing defects are dominant at any specific condition. In a heavily  $(4H)_{Si}^X$  dominated system (such as at low temperature and high pressures)  $rc$  in Eq. 5 is  $\frac{1}{2}$  and thus  $r$  in Eq. 4 should approach 0.5. In a heavily  $(2H)_{Mg}^X$  dominated system (such as at high temperature and low pressures)  $rc$  in Eq. 5 is 1 and thus  $r$  in Eq. 4 should approach 1. The presence of Ti causes complex variations in  $[(2H)_{Mg}^X]$  and thus allows a varied range of  $r$  values that are larger than in Ti-free cases. In the absence of Ti it is difficult for  $r$  to be above 1 as it would require the dominant charge carrier to have less than 2 hydrogen. In Muir et al. (2022) we demonstrated a situation where the concentration exponent for hydrous Mg vacancies is  $\sim 1.2$  (due to the formation of  $H'_{Mg}$ ) but this is only possible in the presence of Al and at low pressures.

Outside of the exponent, the difference between the base diffusion rates of “dry” and “wet” forsterite (e.g. in Eq. 4) vary with pressure and temperature. In dry forsterite,

temperature increases the diffusion rate markedly (due to the  $e^{(-\frac{M}{k_bT})}$  term in determining diffusivity and the increased concentration of intrinsic defects) whereas pressure decreases it slightly (mostly due to a lower number of intrinsic defects being produced). For wet diffusion increasing the temperature increases  $[(2H)_{Mg}^X]$  and diffusivity and thus diffusion rates while increasing the pressure decreases  $[(2H)_{Mg}^X]$  and thus diffusion rates sharply (Table 4). These trends can be seen in Table 5 or Fig. 1.

Outside of pressure and temperature other factors are important to wet Mg diffusion rates. The choice of the buffer will have a strong effect as increasing  $aSiO_2$  increases the favourability of  $(2H)_{Mg}^X$  and thus increases the effect of water on Mg diffusion rates. This is plotted in Fig. S5 where we find in some cases multiple orders of magnitude difference between diffusion rates in MgO or  $MgSiO_3$  buffered system with MgO buffered systems having considerably slower diffusion rates. This is a useful test of the predictions of our model as the predicted differences are large. All results in this work shall be presented with  $MgSiO_3$  buffer as it is closer to the conditions of the mantle.

Ti is present in the study of Fei et al. (2018) and can be an important defect as it can decrease the formation of  $(2H)_{Mg}^X$  in favor of immobile  $\{Ti_{Mg}^{2+}(2H)_{Si}''\}^X$ . Table 6 plots the effect of Ti on Mg diffusion rates where we find that Ti has a large effect at low temperatures and pressures where  $\{Ti_{Mg}^{2+}(2H)_{Si}''\}^X$  is favoured but has little effect on the Mg diffusion rate as temperature or pressure increases.

Al is another important component of forsterite and olivine. As outlined in Muir et al. (2022) Al is not predicted to change the concentration of hydrated Mg vacancies. The presence of Al is predicted to increase the concentration of H-free Mg vacancies but only in dry circumstances (Muir et al. 2020), this effect is suppressed by small amounts of water ( $\sim 5$  wt. ppm) (Muir et al. 2022). Thus we predict that Al should not have a measureable effect on Mg diffusion in wet conditions as it does not change the concentration of diffusing species. Under some conditions, Al can convert  $(2H)_{Mg}^X$  to  $(1H)_{Mg}'$  which will affect the diffusivity. This will speed up Mg diffusion as every 1  $(2H)_{Mg}^X$  can form 2  $H'_{Mg}$  thus doubling the concentration of diffusing species. We do not know the diffusivity of  $H'_{Mg}$  but it is likely between that of  $(2H)_{Mg}^X$  and  $V''_{Mg}$  which will further speed up diffusion as  $(2H)_{Mg}^X$  defects diffuse a lot slower than a  $V''_{Mg}$  defect.

Thus we conclude that while water generally increases Mg diffusion rates the exact amount which it increases the rate and the dependence of this increase on water concentration is highly dependent on the background conditions such as pressure, temperature and crystal composition. Thus



**Table 5** Various outputs from our diffusion model as a function of corrected pressure and temperature

		Dry to wet		Dry ( $[H_2O]_{\text{bulk}} = 0$ wt. ppm)		Wet ( $[H_2O]_{\text{bulk}} = 1\text{--}300$ wt. ppm)			
		Crossover (pure)	Crossover ( $TiO_2 = 500$ wt. ppm)	log A	log Anisotropy	log A	log B	r	log Anisotropy
1000 K	0 GPa	0.00	0.00	- 24.41	1.20	- 18.15	- 18.10	0.56	3.81
	5 GPa	0.00	0.00	- 25.29	0.44	- 19.97	- 19.99	0.55	4.95
	10 GPa	0.00	0.00	- 25.33	0.14	- 22.86	- 22.91	0.55	5.96
1500 K	0 GPa	0.00	0.01	- 17.90	0.80	- 15.33	- 14.84	0.65	2.04
	5 GPa	0.00	0.00	- 18.78	0.60	- 15.82	- 15.80	0.56	2.89
	10 GPa	0.00	0.00	- 19.96	0.57	- 18.34	- 18.36	0.56	3.40
2000 K	0 GPa	0.58	0.81	- 14.51	0.63	- 14.34	- 14.13	0.88	1.98
	5 GPa	0.35	0.56	- 15.26	0.48	- 14.45	- 14.48	0.67	2.82
	10 GPa	0.85	1.41	- 16.32	0.56	- 15.68	- 15.69	0.56	3.28

The first two columns show the concentration (in wt. ppm) of  $[H_2O]_{\text{bulk}}$  where we convert from the “dry” regime to a “wet” regime defined as the point of inflection in an anisotropy curve such as in Fig. 3. This is shown for a “pure” forsterite and one containing 500 wt. ppm  $TiO_2$ , the value is similar and small in both cases. The final 6 columns concern diffusion rates in “pure” (Ti-free) forsterite with Ti-bearing forsterite shown in Table 6. The first two columns concern dry forsterite with no H-bearing defects and show the diffusion rate (A in Eq. 4) and the anisotropy  $[D_{[001]}/D_{[110]}]$ . The last 4 columns concern forsterite with H-bearing defects. We show the results of fitting to Eq. 4 between  $[H_2O]_{\text{bulk}} 1$  to 300 wt. ppm (the “wet” region)- for the purposes of fitting we used  $[H_2O]_{\text{bulk}} = [H_2O]_{\text{bulk}}^{-1}$  so that A in these cases reflects diffusion at 1 wt. ppm  $[H_2O]_{\text{bulk}}$ . The final column shows the anisotropy of the wet system

**Table 6** Plot of fits to dry and wet forsterite (as in Table 5) with varying amounts of  $TiO_2$  added at different T and P

		0 GPa				5 GPa				10 GPa			
$TiO_2$ (wt. ppm)		log A (dry)	log A	log B	r	log A (dry)	log A	log B	r	log A (dry)	log A	log B	r
1000 K	0	- 24.22	- 18.15	- 18.10	0.56	- 25.29	- 19.97	- 19.99	0.55	- 25.33	- 22.86	- 22.91	0.56
	100	- 24.22	- 19.72	- 19.15	1.09	- 25.29	- 20.36	- 20.00	0.58	- 25.33	- 22.93	- 22.89	0.56
	500	- 24.22	- 20.26	- 21.11	1.63	- 25.29	- 21.60	- 21.29	1.02	- 25.33	- 23.21	- 22.81	0.56
1500 K	0	- 17.90	- 15.33	- 14.84	0.65	- 18.78	- 15.82	- 15.80	0.56	- 19.96	- 18.34	- 18.36	0.56
	100	- 17.90	- 15.83	- 15.42	0.95	- 18.78	- 16.08	- 15.88	0.59	- 19.96	- 18.36	- 18.32	0.55
	500	- 17.90	- 16.34	- 15.99	1.08	- 18.78	- 16.83	- 16.47	0.96	- 19.96	- 18.41	- 18.32	0.55
2000 K	0	- 14.51	- 14.34	- 14.13	0.88	- 15.26	- 14.45	- 14.48	0.67	- 16.32	- 15.68	- 15.69	0.56
	100	- 14.51	- 14.39	- 14.29	0.95	- 15.26	- 14.57	- 14.55	0.77	- 16.32	- 15.73	- 15.69	0.56
	500	- 14.51	- 14.61	- 14.68	1.05	- 15.26	- 14.75	- 14.66	0.93	- 16.32	- 15.77	- 15.69	0.55

Anisotropy is not affected by the addition of Ti and is presented in Table 5

when quantifying the effect of water on forsterite diffusion rates- and the rates of properties dependent upon diffusion-measurements need to be made at the conditions in which you are interested as extrapolating to these conditions is not straightforward.

**Diffusional anisotropy**

As well as an increase in Mg diffusion rate we also predict that the presence of water will lead to a sharp increase in diffusional anisotropy. Anisotropy is shown for a sample composition in Fig. 3 though all compositions have similar

traces with the values explored in Table 5. At low water contents in the “dry” diffusion regime diffusion and its anisotropy are controlled by  $V''_{Mg}$  and  $Mg_I^{**}$ . At high water contents in the “wet” diffusion regime diffusion and its anisotropy is controlled primarily by  $(2H)_{Mg}^X$ . Inside each regime the anisotropy of diffusion comes from the anisotropy of the diffusion coefficients of  $V''_{Mg}$  and  $Mg_I^{**}$  or  $(2H)_{Mg}^X$  and thus is sensitive to temperature and pressure but insensitive to water and Ti concentration. Increasing the temperature decreases the anisotropy, increasing the pressure increases it. As  $(2H)_{Mg}^X$  has highly anisotropic diffusion favouring the [001] direction (Table 3) Mg diffusion in the wet region is highly

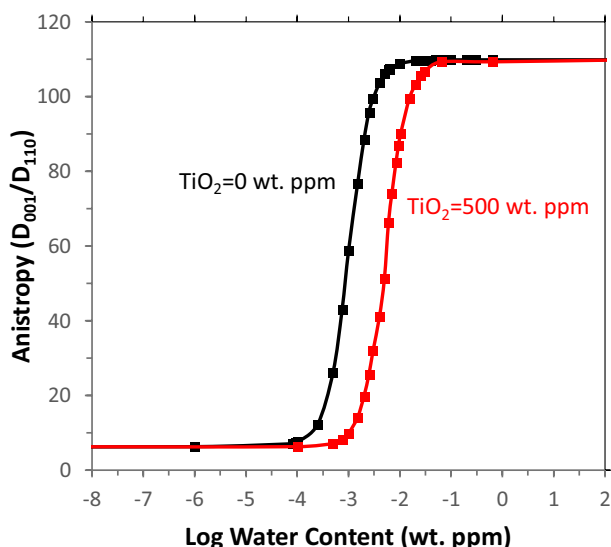


**Fig. 3** The anisotropy of diffusion [ $D_{[001]}/D_{[110]}$ ] as a function of water content at 1500 K and 0 GPa corrected and with and without  $\text{TiO}_2$ . At low water contents a “dry” regime persists in which anisotropy is low, at high water contents a “wet” regime in which anisotropy is high. In both regimes the anisotropy is insensitive to water content, only varying in a small transition window between them. All pressure and temperatures gave similar plots with some numbers listed in Table 5

anisotropic favouring the [001] direction. The anisotropy of diffusion is listed in Table 5 with wet forsterite possessing Mg diffusion that is 1–4 orders of magnitude more anisotropic than dry forsterite. We are not aware of any experimental measures of the anisotropy of Mg diffusion in wet forsterite but this would be a good test of our model as the effect is very large particularly at low temperatures.

We predict very strong Mg diffusional anisotropy in wet forsterite. It could be argued that our model lacks some mechanism that exists in real forsterite to mitigate this anisotropy but it is difficult to propose what such a mechanism could be. While our errors are largely unknown as discussed in the methods our ability to replicate experimental values (Figs. 2 and 4) suggests that our diffusion mechanism is at least broadly correct and can produce the signals observed experimentally. For dry forsterite, the simple hop mechanism can also reproduce experimentally observed diffusion rates (Muir et al. 2021, 2020). Our simple hop mechanism is an available pathway in a real crystal and thus any alternative mechanism must compete with it and needs similar or lower activation enthalpies (to ensure it can compete) than the controlling hop of our mechanism ( $\sim 1.26$  eV) without activation enthalpies being too low (which will lead to faster diffusion than observed experimentally).

In our model, we have ignored any multiatom diffusion mechanisms but these are all likely to have much higher

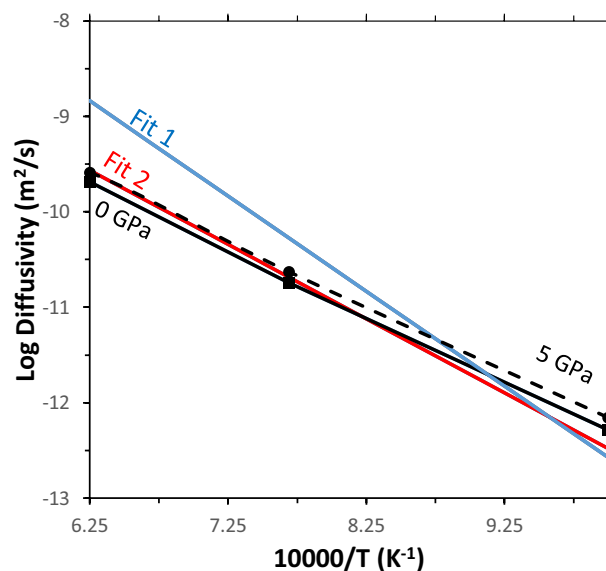


**Fig. 4** Comparison of  $D_{Mg}^{Hvac}$  (diffusivity of  $(2H)_{Mg}^x$ ) calculated in this study at 2 corrected pressures and 4 temperatures (1000, 1300, 1600 and 2000 K) compared to a value determined from fitting a model to experimental data for H diffusion obtained from Michael Jollands (personal communication, 2021)

activation enthalpy barriers than 1.26 eV. By the nature of the forsterite crystal structure, any hops from any atom/site which is not a hop along an [001] Mg M1 chain has to move through a more crowded space than the [001] Mg M1 chain hop and thus likely has a higher activation enthalpy. This is precisely what we have observed for Mg vacancy hopping (Table 3). A multi-atom diffusion path will still need to move atoms through such crowded space at some point and thus likely will have higher activation barriers than the simple hop. Two obvious multisite mechanisms which could increase diffusional isotropy would be coupling Mg vacancies with either Si or O sites and diffusing through these sites. The first is very unlikely because moving an Mg vacancy to an Si site will lead to an increase in charge ( $V_{Si}''$  transforms into  $V_{Si}''''$  and  $Si_{Mg}^{2\bullet}$  or  $(2H)_{Mg}^x$  leads to  $(2H)_{Si}''$  and  $Si_{Mg}^{2\bullet}$ ) which will sharply increase coulombic repulsion terms. The second is also unlikely ( $V_{Mg}''$  leads to  $V_O''$  and  $Mg_O''''$ ) because it will lead to an increase in charge and because the O site is too small to contain Mg atoms effectively.

One diffusion mechanism that could possess low activation enthalpies and more isotropic diffusion is for  $(2H)_{Mg}^x$  to convert into another species such as  $(4H)_{Si}^x$  which then diffuses and converts back to  $(2H)_{Mg}^x$ . Si site diffusion is relatively isotropic (Costa and Chakraborty 2008) and so such a mechanism would likely reduce the predicted anisotropy. While we have considered the conversion of  $(2H)_{Mg}^x$  into  $(4H)_{Si}^x$  in our model we do not consider  $(4H)_{Si}^x$  diffusion.  $(4H)_{Si}^x$  likely diffuses orders of magnitude slower than  $(2H)_{Mg}^x$

based on observations of hydrogen diffusion (Padron-Navarta et al. 2014) and when combined with the conversion rates of  $(2H)_{Mg}^X$  into  $(4H)_{Si}^X$  and back this mechanism is likely negligible when considering Mg diffusion rates but we cannot directly rule it out. The presence of such a mechanism could be tested by determining diffusion rates against the ratio of  $(2H)_{Mg}^X:(4H)_{Si}^X$  (by for example changing the buffer or the pressure).

One final possibility which is not considered in our model is the effect of macroscopic defects in the crystal. Very small forsterite crystals which have relatively large defective regions such as grain boundaries and dislocations could potentially change the diffusion pathways towards these regions which could increase the isotropy of Mg diffusion. This is energetically plausible but would lead to a diffusion anisotropy that is dependent upon crystal size/quality which seems unlikely.

## Discussion

The main conclusion of this work is that water increases the rate and the anisotropy of Mg diffusion in forsterite but that the magnitude of this effect is highly dependent upon the prevailing conditions.

## Comparisons to experiments

In Fig. 2 we compare our Mg diffusion rates with those obtained by Fei et al. (2018). We find a good match between our values and those of Fei et al. (2018) at higher water contents but an increasing mismatch with lower water contents. This is unsurprising as when we consider the high pressures conditions of the experiments, we predict that water is overwhelmingly in  $(4H)_{Si}^X$  defects. We predict that at these conditions water in  $(2H)_{Mg}^X$  defects makes up between 0.01 and 0.2% of the total water content (with this number decreasing with increasing  $[H_2O]_{bulk}$ ) which is also observed by the lack of an identifiable  $(2H)_{Mg}^X$  peak in the FTIR signal presented in Fei et al. (2018). Thus very small errors in determining the total water content, the pressure or the temperature would lead to large errors in relative  $[(2H)_{Mg}^X]$  concentration which becomes increasingly more important as water concentration decreases. Kinetics could also be an issue in the experiment. We predict that most water in forsterite in high pressure conditions resides in  $(4H)_{Si}^X$  defects. The production of  $(4H)_{Si}^X$  reduces Mg diffusion rates by reducing  $[(2H)_{Mg}^X]$ . We predict, however, that the production of  $(4H)_{Si}^X$  occurs through a reaction involving the interaction of 2  $(2H)_{Mg}^X$  defects and thus its rate is also dependant on Mg diffusion rates. Thus the distribution and the diffusion of  $(2H)_{Mg}^X$  likely operate

on similar timescales though this should be less of an issue at the long time scales of the mantle where thermodynamic equilibration is likely. Experiments done at low pressures and high temperature should be less impacted by such concerns as a larger proportion of the water is predicted to be taken up by  $(2H)_{Mg}^X$  defects in these conditions.

Fei et al. (2018) found an exponent  $r$  of  $\sim 1.2$  at 1300 K and 8 GPa. We predict this exponent to be much lower ( $\sim 0.6$ ) even in the presence of Ti. Our distribution model predicts that under these conditions most water would be in  $(4H)_{Si}^X$  which also appears to be the case from the IR spectra in Fei et al. (2018) which shows a large peak at  $\sim 3610$  and some bands between 3450 and 3600  $cm^{-1}$  which are generally attributed as  $(4H)_{Si}^X$  bands (Tollan et al. 2017). When  $(4H)_{Si}^X$  is the dominant H-bearing defect it is extremely difficult for the water diffusion exponent  $r$  to rise above 1 as this would generally require the relevant diffusing species to have more than 4 H atoms in its structure. Even if  $(4H)_{Si}^X$  diffusion contributes significantly to Mg diffusion rates then  $r$  would be close to but below 1 assuming a linear relationship between  $[(4H)_{Si}^X]$  and diffusion rate. If the experimental  $r$  value of 1.2 is correct then this is an indication that some more complex mechanism is present which would also explain the increasing mismatch we see between theoretical and experimental diffusions as  $[H_2O]_{bulk}$  decreases. In general we expect the value of  $r$  to be quite dependent upon crystal composition and experimental makeup as the ratio of  $[(2H)_{Mg}^X]$  to  $[H_2O]_{bulk}$  is quite dependent upon these variables (Muir et al. 2022). Thus a series of measurements of the  $r$  in different conditions would be strong evidence for or against our model.

To examine the accuracy of our calculations we can also compare our diffusivity with that obtained experimentally for hydrogen in forsterite. In iron-free systems, the diffusion of hydrogen is expected to be controlled largely by  $(2H)_{Mg}^X$  diffusion as it is the fastest diffusing hydrogen species (Padron-Navarta et al. 2014). Measuring this diffusion is complicated by the fact that the distribution of hydrogen can vary in different conditions and during diffusional processes different H-bearing defects can convert into one another. This has recently been examined by Michael Jollands (personal communication, 2021) who built a combined distribution and diffusion model for hydrogen in forsterite. According to this model  $(2H)_{Mg}^X$  diffusivity is at least an order of magnitude higher than previously measured (generally by fitting to Fick's second law) as  $(2H)_{Mg}^X$  undergoes conversions to different H-bearing defects which slows the apparent rate when simply measuring concentration profiles. In Fig. 4 we show a comparison between our calculated diffusivities and those determined from the model and find strong agreement. Our calculated diffusivities are around an order of magnitude higher than

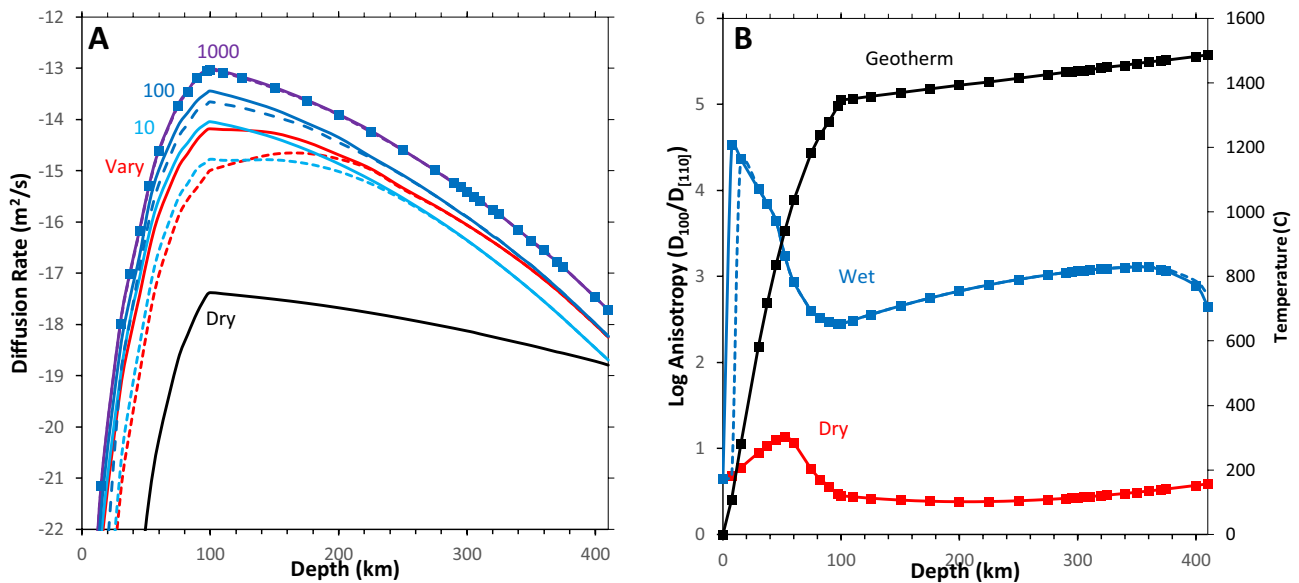


**Fig. 5** **A** Diffusion rate and **B** Anisotropy of diffusion  $[D_{100}/D_{110}]$  of Mg along an oceanic geotherm (pictured in black on the secondary  $x$ -axis of B, taken from Green and Ringwood 1970). **A** Solid and dashed lines represent “pure” forsterite and forsterite with 500 wt. ppm TiO<sub>2</sub>, respectively. The black line contains no H-bearing defects, while shades of blue contain fixed amounts of H-bearing defects (given as  $[H_2O]_{\text{bulk}}$  in wt. ppm) and red lines have a varying amount of water content with depth  $[H_2O]_{\text{bulk}} = (3 + 1.6 \times 10^{-4} z^{2.2})$  taken from Demouchy and Casanova (2016) where  $z$  is depth in km.

**B** Dry forsterite is shown in red, wet forsterite is shown in blue with the solid line representing no TiO<sub>2</sub> and the dashed line with 500 wt. ppm TiO<sub>2</sub>. All amounts of water above 1 wt. ppm produce an identical trace to the varied water curves pictured here (and thus are not shown) as discussed in the text. Values below 50 km require extrapolation below 1000 K and thus are potentially unreliable. Values for all sample were calculated for the temperature and depth points shown in (B) and 1000 wt. ppm  $[H_2O]_{\text{bulk}}$  and then plotted as a line

previously measured diffusivities such as in Sun et al. (2019) that were determined directly from fitting Fick’s law for the reasons stated above. Some differences are expected as the experimental model includes all methods of hydrogen diffusion whereas we only consider  $(2H)_{Mg}^X$  but the strong match between our calculated data and the model fit to experiments by Michael Jollands suggests both that  $(2H)_{Mg}^X$  diffusivity largely controls hydrogen diffusivity in real forsterite (and that contributions from  $(4H)_{Si}^X$  and  $\{Ti_{Mg}^{2+}(2H)_{Si}^{''}\}^X$  can be ignored) and that our calculations accurately calculate its diffusivity.

### Diffusion rates in upper mantle conditions

The main conclusion of this work is that water increases the rate and the anisotropy of Mg diffusion in forsterite but that the magnitude of this effect is highly dependent upon the prevailing conditions. Thus we stress that the effect of water on Mg diffusion must be measured and constrained in the relevant conditions as extrapolation is extremely difficult. Even then it will be difficult to fit the effect of water to simple relationships across geophysically relevant P and T ranges.

To demonstrate the complexity of controls of Mg diffusivity we projected our results along with one relevant P and T range, an oceanic geotherm, with the results shown in Fig. 5. We predict that water has a varied effect on Mg diffusion with depth. In the shallow upper mantle, water is predicted to cause a large (up to 4 orders of magnitude for 100 wt. ppm water) increase in diffusion rate which increases with depth before peaking at ~100 km. As depth increases the effect of water decreases until 410 km where even an extremely wet forsterite (1000 wt. ppm) has an Mg diffusion rate that is less than 1 order of magnitude higher than dry forsterite. This varying behaviour is due largely to variations in  $[(2H)_{Mg}^X]$  which initially increases, peaks at 100 km then decreases sharply in favour of  $[(4H)_{Si}^X]$  (Muir et al. 2022). The presence of even large amounts of Ti decreases the maximum diffusion rate of Mg in wet forsterite but not to a large degree. The effect of  $[H_2O]_{\text{bulk}}$  on Mg diffusion rates is thus varied, complex and changes with depth.

Water is predicted to also induce large differences in the anisotropy of Mg diffusion with “wet” forsterite generally being 2–3 orders of magnitude more anisotropic than dry samples (Fig. 5). As discussed above anisotropy is insensitive to water content above a small value of  $[(2H)_{Mg}^X]$  which is likely exceeded in wet samples in the upper mantle and thus all concentrations of water will lead to identical diffusional

anisotropy. Our predicted anisotropy of Mg diffusion in Fig. 5 has many peaks and features based on temperature and pressure variations which will vary significantly with thermal fluctuations but the effect of water on increasing anisotropy is robust up until the final ~ 10 km of the lower mantle where  $[(2H)_{Mg}^X]$  concentrations are predicted to decrease sharply and so the anisotropy of diffusion is also predicted to decrease sharply.

It is important to emphasise that these studies lack iron which would affect conclusions in olivine. The primary way this could happen is that iron could reduce the amount of  $(2H)_{Mg}^X$  that is formed by allowing the formation of alternative hydrogen complexes- primarily  $\{Fe_{Mg}^{\bullet} H'_{Mg}\}^X$  (Berry et al. 2007). This will reduce the effect of water on Mg diffusion rates. The trends with pressure, temperature, buffer activity and Ti concentration should all remain largely intact however unless iron-hydrogen complexes are strongly favoured in all conditions such that water produces no  $(2H)_{Mg}^X$  and doesn't increase diffusion rates. The predicted increase in Mg diffusional anisotropy in particular is insensitive to the amount of water above a small value and thus unless Fe complexes drastically reduce the value of  $[(2H)_{Mg}^X]$  we predict Mg diffusion in wet olivine to remain very anisotropic. Thus the trends seen in diffusion speed and anisotropy with depth in wet forsterite should remain in wet olivine and throughout upper mantle conditions water will affect diffusion rates differently and no one simple water effect will be present.

**The effect of Mg diffusion rate variations on electrical conductivity**

As an example of how these properties affect the upper mantle, we calculated one key property that is controlled in part by Mg diffusion, electrical conductivity. Previously the observed conductivity of olivine has been explained with a model that combines three major mechanisms: proton-polaron hopping, Mg vacancy hopping and some hydrous factor (Gardes et al. 2014). The exact nature of the hydrous factor is unknown with some work speculating that it is due to  $(2H)_{Mg}^X$  diffusion (Fei et al. 2018).  $(2H)_{Mg}^X$  and  $(4H)_{Si}^X$  formally have no charge and thus generally their diffusion does not contribute to conductivity. As argued by Fei et al. (2018) if there is an exchange between  $(2H)_{Mg}^X$  and  $V''_{Mg}$  then the diffusion of  $(2H)_{Mg}^X$  contributes to the movement of charge carriers and thus conductivity and an identical argument could be made about  $(4H)_{Si}^X$  and  $V''''_{Si}$ . We therefore built a model to test this hypothesis and to examine whether our Mg diffusion rates could explain observed conductivity in olivine.

We predicted conductivity using the assumption of parallel conduction via the following equation:

$$\begin{aligned} \sigma = & \sigma_0^{Polaron} e^{-\frac{\Delta H^{Pol}}{RT}} + \frac{D^*_{vac} \times [V''_{Mg}]}{RT} \times (2 \times F)^2 \\ & + \frac{D^*_{int} \times [Mg_I^{\bullet\bullet}]}{RT} \times (2 \times F)^2 \\ & + \frac{D^*_{HMgVac} \times [(2H)_{Mg}^X]}{RT} \times (2 \times F)^2 \\ & + \frac{D^*_{HSivac} \times [(4H)_{Si}^X]}{RT} \times (4 \times F)^2 \end{aligned} \tag{6}$$

with activation enthalpies in kJ/mol, concentrations in mol/m<sup>3</sup> and F is the Faraday constant.  $\sigma_0^{Polaron}$  is the conductivity coefficient for polaron conduction and  $\Delta H^{Pol}$  is the enthalpy coefficient for polaron conduction. The first term refers to proton-polaron hopping. We have not calculated this and have taken values for these terms directly from Gardes et al. (2014). The next 4 terms refer to the diffusion of Mg vacancies, Mg interstitials,  $(2H)_{Mg}^X$  and  $(4H)_{Si}^X$ , respectively with conductivity calculated from the Nerst-Einstein equation. In the formulation of Gardes et al. (2014) there was no diffusion term for Mg interstitials but we find that Mg vacancies and Mg interstitials have similar diffusion rates in dry forsterite (Muir et al. 2021) and thus this term should be included. The parameters for all diffusion terms were taken from this work except for the diffusivity of  $(4H)_{Si}^X$  which we have not calculated. Diffusivity was set to  $D^*_{HSivac} = 10^{3.3} \exp[-\frac{461}{RT}]$  taken from Padron-Navarta et al. (2014). This term lacks a pressure derivative and likely represents some combination of inherent  $(4H)_{Si}^X$  diffusivity and the rate of  $(4H)_{Si}^X$  converting to  $(2H)_{Mg}^X$ , diffusing and then converting back but this is not a major component of the conductivity (see M3 vs M4 in Fig. S6) and thus the exact diffusivity of  $(4H)_{Si}^X$  doesn't change our overall conclusion. We have neglected the diffusion of Si and O vacancies in our model as their concentrations are predicted to be very small ( $< 1 \times 10^{-15}$  defects/fu) and thus irrelevant when considering the effects of water. Any  $\{Ti_{Mg}^{\bullet\bullet} (2H)_{Si}''\}^X$  that is produced was considered immobile and thus non-conductive for the reasons discussed above.

The exchange hypothesis above would introduce an extra step to the “diffusion of charge carriers” and the exchange rate between  $(2H)_{Mg}^X$  and  $V''_{Mg}$  would be important in this scenario. We have assumed that this exchange step is very fast and that the rate-limiting step is the diffusion of  $(2H)_{Mg}^X$  and/or  $V''_{Mg}$  and thus any exchange kinetics can be ignored. This may not be accurate but in this way we have assumed the maximum conductivity from this mechanism as any exchange kinetics will effectively slow down the diffusion of charge carriers and thus reduce conductivity. As will be seen even with this assumption (and other assumptions that maximise conductivity such as ignoring the effect of iron as



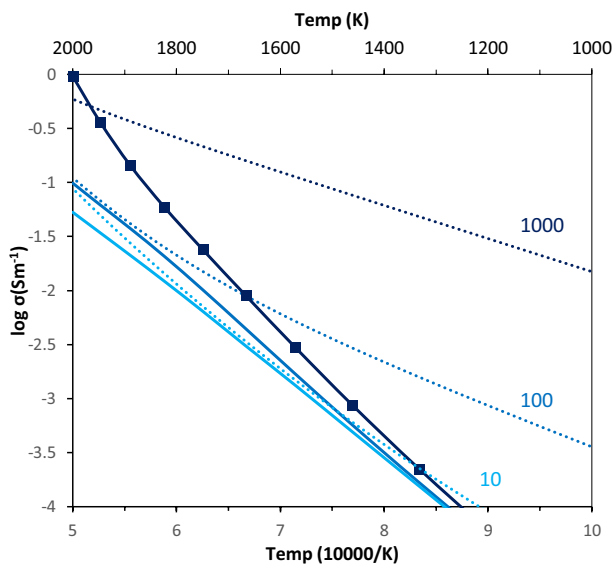


**Fig. 6** Plot of conductivity vs temperature for different water concentrations (10, 100 and 1000 wt. ppm). Solid lines are our prediction using Eq. 6 in the text, the dotted lines are the G14 model which was determined from Eq. 1 and Table 1 in Gardes et al (2014). In Fig. S2 we show the results of different modifications to Eq. 6 but none of them are close to matching the model of G14. Pressure was set to 0 GPa corrected, the effect of pressure is shown in Fig. S3. Our values in this plot were constructed by calculating the conductivity every 100 K and plotting the points as a line

discussed below) our predicted conductivity is too small rather than too large. Thus, as argued later, it is likely that the diffusion of  $(2H)_{Mg}^X$  and  $(4H)_{Si}^X$  do not contribute to conductivity as they do not carry a charge and that the effect of water on conductivity is through another mechanism.

In Fig. 6 (with a 2D plot of conductivity in Fig. S7) we plot our predicted conductivity vs those determined from the model in Gardes et al. (2014) (G14). The G14 model correctly replicates a range of experimental observations and thus a model that matches G14 also matches experimental observations. The most important fact is that our model predicts very different conductivities from G14 and generally lower conductivities even though our model likely

overpredicts conductivity as discussed above. This misfit is largest at low temperatures where proton-polaron conductivity should be dominant. This is a curious result as our proton-polaron numbers are taken directly from G14 and so it would be expected that our fitting would be better at low temperature and worse at high temperature where we find some weak agreement between our model and G14. This mismatch is due to the low activation enthalpy of the water component of G14 ( $< 100$  kJ/mol) which means it must be strong at low temperatures whereas our water component—the diffusion of  $(2H)_{Mg}^X$ —is only strong at high temperature. The water component in G14 has a lower activation enthalpy than even the proton-polaron component ( $\sim 145$  kJ/mol) and thus must be the primary low temperature mechanism. It is suggested by Gardes et al. (2014) that the water mechanism could be due to the electronic effects of the water due to its low activation enthalpy but based on speculation with no evidence.

In Table 7 we compare activation enthalpies for the water part of G14 with those predicted in our model. Our activation enthalpies are considerably higher. It is important to clarify the term “activation enthalpy”. In a diffusion mechanism, there are at least 2 “activation enthalpies”—one for hopping of the defects (Table 2) and one for production of the defects (Table 4)—and in a hydrated system where the concentration and mobility of  $(2H)_{Mg}^X$  are both strong functions of temperature both of these are important. If ionic diffusion is important to olivine conductivity at least 2 activation enthalpies are likely required to model the effect of water. In experimental fittings of diffusion or conductivity with temperature these two features will be combined into a single “activation enthalpy” which we have done in Table 7 with the first four columns showing a “normal” activation enthalpy containing two parts and the final column showing an activation enthalpy with a fixed  $(2H)_{Mg}^X$  concentration thus removing the production of defects component. In either case, our predicted activation enthalpy for the water component is much higher than that of G14 and a diffusion-based mechanism is unlikely to ever have activation enthalpies  $< 100$  kJ/mol.

**Table 7** Comparison of the activation enthalpy (in kJ/mol) in three directions for the hydrous part of the conductivity fit in Gardes et al. (2014) with that determined in this work at 0 GPa (corrected)

	Gardes (2014)		This work				
	Fit 1 ( $r=1/3$ )	Fit 2 ( $r=1.99$ )	1 wt. ppm	10	100	1000	10 (all $(2H)_{Mg}^X$ )
	$\Delta H^{\text{Hyd}}$	$\Delta H^{\text{Hyd}}$	$\Delta H^{\text{Hyd}}$	$\Delta H^{\text{Hyd}}$	$\Delta H^{\text{Hyd}}$	$\Delta H^{\text{Hyd}}$	$\Delta H^{\text{Hyd}}$
[100]	92	66	299.64	283.77	273.55	260.86	348.75
[010]	95	104	367.38	346.67	324.35	278.70	336.99
[001]	81	61	377.20	353.38	327.66	279.30	268.45

Two fits from Gardes et al. 2014 are shown with different water exponents ( $r$ ). To determine our activation enthalpy we determined conductivity between 800 and 2000 K while setting the polaron term in Eq. 6 to 0 and then fit an equation of the form  $\sigma = ae^{-b/RT}$  where  $a$  and  $b$  are fitting parameters. This was done at multiple different values of  $[H_2O]_{\text{bulk}}$ . The final column represents  $[H_2O]_{\text{bulk}} = 10$  wt. ppm but with all water fixed as  $(2H)_{Mg}^X$

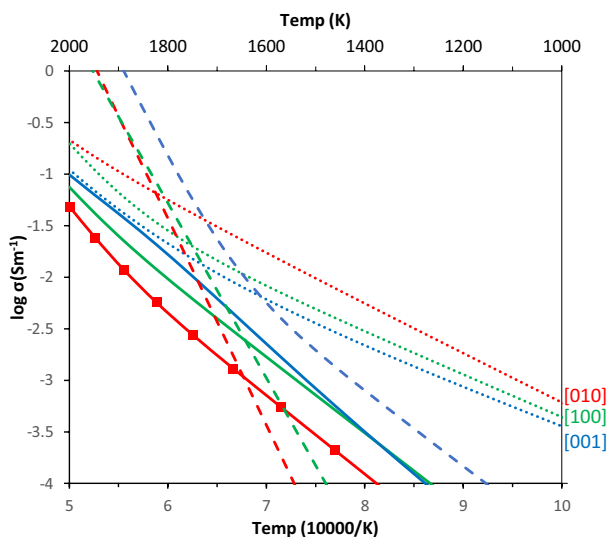


**Fig. 7** Comparison of conductivity in three directions (red=[010], green=[100], blue=[001]) against temperature determined from Eq. 6 in our model (solid lines) vs those determined from G14 (dotted lines) and from Fei et al. (2020) (dashed lines) determined from Eq. 9 and Table 3.  $[\text{H}_2\text{O}]_{\text{bulk}}$  was set to 100 wt. ppm and pressure to 0 GPa (corrected). Our predicted diffusional anisotropy is close to the reverse of that determined by Gardes et al. (2014) while we match the same order as in Fei et al. (2020). Our values in this plot were constructed by calculating the conductivity every 100 K and plotting the points as a line

A further problem comes when you consider different water concentrations- the misfit between our model and that of G14 is highly variable and depends upon  $[\text{H}_2\text{O}]_{\text{bulk}}$ . This strongly suggests our model does not correctly represent how water affects olivine conductivity as a correct mechanism should scale with  $[\text{H}_2\text{O}]_{\text{bulk}}$  in a way that replicates experimental observations which are matched by the model of G14.

This mismatch can also be seen in the water concentration exponent  $r$  which is different between our model and G14. In the case of conductivity being proportional to  $(2H)_{\text{Mg}}^X$  diffusion then  $r$  should be equal to that for Mg diffusion in Table 5. Gardes et al. (2014) found two good fits with the favoured one having  $r = 1/3$  and the less favoured one  $r = 1.99$ . Neither of these fit either our  $r$  values in Table 5 or  $r$  values that can be easily achieved when considering mechanisms for producing  $(2H)_{\text{Mg}}^X$ . If  $(4H)_{\text{Si}}^X$  is considered to be the controlling species for conductivity then  $r = 2$  in some cases (Kohlstedt 2006; Muir et al. 2022) but this is difficult to reconcile with the slow diffusion rate of  $(4H)_{\text{Si}}^X$  (Padron-Navarta et al. 2014) even if it is the dominant water species.

There are many other inconsistencies between our model and that of G14. As shown in Fig. 7 our predicted anisotropy of conduction is opposite to that of G14 even at high temperatures where a diffusion mechanism, which

favours [001] conduction, would be predicted to be strong. The preservation of conductivity favouring an [010] anisotropy even at high temperatures in the G14 model is evidence that something other than a diffusive vacancy mechanism is important in wet olivine conduction.

In this work, we have not calculated the effect of iron. We include the effect of polarons which arise from iron but through the fitting from Gardes et al. (2014). Iron will have some effect on  $V_{\text{Mg}}''$  through Mg-Fe interdiffusion effects but the overall rate of Mg self and Mg-Fe interdiffusion is similar (Chakraborty, 2010) and thus this is not an explanation for the conductivity differences predicted here. Fe can allow the formation of trivalent compounds with water, likely  $\{\text{Fe}_{\text{Mg}}^{\bullet} \text{H}_{\text{Mg}}'\}^X$  (Berry et al. 2007). This defect contains two charge carriers  $\text{Fe}_{\text{Mg}}^{\bullet}$  and  $\text{H}_{\text{Mg}}'$  but we calculate the binding energy of this pairing to be 2.3–2.8 eV at 1500 K and from 0 to 10 GPa and thus these 2 charge carriers are strongly bound to each other and unlikely to diffuse. The formation of  $\{\text{Fe}_{\text{Mg}}^{\bullet} \text{H}_{\text{Mg}}'\}^X$  will reduce the concentration of  $(2H)_{\text{Mg}}^X$  and  $(4H)_{\text{Si}}^X$  and thus further reduce conductivity and increase the mismatch between our diffusive model and reality. Experimental evidence also suggests that Fe-hydrogen complexes are unlikely to be contributors to conductivity. These complexes are expected to involve ferric iron and thus if they contributed strongly to conductivity, conductivity would be expected to increase with increasing oxygen fugacity which converts ferrous iron to ferric iron and thus would be expected to increase the concentration of ferric-hydrogen complexes. In Dai and Karato (2014), however, it was found that conductivity is inversely proportional to oxygen fugacity. This relationship suggests that ferrous iron is a stronger contributor to conductivity than ferric iron. Thus the presence of iron in olivine samples will not explain the conductivity discrepancies found here.

Similar to iron the presence of Ti can form  $\{\text{Ti}_{\text{Mg}}^{\bullet\bullet} (2H)_{\text{Si}}''\}^X$  which is likely immobile. This will reduce the concentration of  $(2H)_{\text{Mg}}^X$  and  $(4H)_{\text{Si}}^X$  (Muir et al. 2022) and thus the conductivity even further. This is in contrast to measurements by Dai and Karato (2020) where it was found that Ti increases conductivity in water-poor regions where  $\{\text{Ti}_{\text{Mg}}^{\bullet\bullet} (2H)_{\text{Si}}''\}^X$  is important and has little effect in water-rich regions where  $\{\text{Ti}_{\text{Mg}}^{\bullet\bullet} (2H)_{\text{Si}}''\}^X$  is unimportant. For Ti to increase conductivity in an ionic regime  $\{\text{Ti}_{\text{Mg}}^{\bullet\bullet} (2H)_{\text{Si}}''\}^X$  would have to diffuse quickly which we find to be unlikely and so this is further evidence that the mechanism by which water increases conduction in olivine is not ionic diffusion.

Finally, in Fig. S6 we add/remove different parts to Eq. 6 and consider the case of  $\text{H}_{\text{Mg}}'$  produced by Al to examine how

each part of Eq. 6 modifies the final conductivity but in no case do we find anything that closely matches the G14 model.

The very different behaviour predicted by our model compared to that of Gardes et al. (2014), which matches experimental observations, is evidence that our model is incorrect. This is perhaps unsurprising as our model relies upon the diffusion of  $(2H)_{Mg}^X$  and  $(4H)_{Si}^X$  which are formally not charge carriers. Previously it has been suggested that water produces interstitial hydrogen ( $H_i^*$ ) which is a charge carrier and that it is the diffusion of  $H_i^*$  that explains the conductivity (Sun et al. 2019; Karato 2013). As shown in Table 5 and discussed more in Muir et al. (2022) our calculations predict that  $H_i^*$  is unlikely to form in significant concentrations particularly at high water concentrations. A further argument against  $H_i^*$  diffusion being the important factor is that our mismatch with G14 is highest at low temperatures.  $H_i^*$  is favoured by high temperatures because it has more configurational entropy than other H-bearing defects. Thus if our model simply missed a  $H_i^*$  diffusion factor we would expect better matches to G14 at low temperature and worse matches at high temperatures which is the opposite of what we observe. Measurements of  $H_i^*$  diffusion rates also lead to higher activation enthalpies and different anisotropy values than have been seen in G14 (Kohlstedt and Mackwell 1998).

In Fig. 7 we compare our results to another model, that of Fei et al. (2020). This model was constructed from high-temperature measures of conductivity and thus was designed to more accurately capture the high-temperature mechanism of conductivity which is expected to be ionic conduction. The activation enthalpy of the water mechanism in this work was found to be 337 kJ/mol along the [100] direction, 396 kJ/mol along the [010] and 385 kJ/mol along the [001]. These are generally higher than the values we found in Table 7, the opposite problem with the comparison to G14. As can be seen in Fig. 7 the model of Fei et al. (2020) produces anisotropies in the same order ([001] > [010] > [100]) as in our work but with extremely different temperature dependence that doesn't fit our predictions at all.

All of these problems combined mean that is very unlikely that the contribution of water to olivine conductivity is through bulk  $(2H)_{Mg}^X$  or  $(4H)_{Si}^X$  diffusion. A more likely explanation is that water has an electronic effect on conductivity by adding donor or acceptor states to the bandgaps as has been seen in oxide semiconductors (McCluskey et al. 2012) or alternatively water could affect grain boundary diffusion which could be important in olivine conductivity (Han et al. 2021). As our model increasingly diverges from that of G14 as temperature decreases either the new mechanism for the effect of water on conductivity must be strong at low temperatures or the polaron mechanism must be stronger than is predicted in G14 and the water mechanism weaker. These are clear fitting tradeoffs and an alternative fit that assigns

strong values to the proton-polaron mechanism at a lower temperature would solve some of these unresolved issues but this would require lowering the activation enthalpy of the proton-polaron component (~ 141–146 kJ/mol) to likely be below 100 kJ/mol (the activation enthalpy of the water component in G14). A similar activation enthalpy for the proton-polaron component has been determined, however, in both dry (141 kJ/mol Dai et al. (2010)) (160 kJ/mol Constable et al. (1992)) and wet conditions (165 kJ/mol Yoshino et al. (2009), generally 120–160 kJ/mol though in 2 runs < 100 kJ/mol Fei et al. (2020)). This suggests the proton-polaron assignment in G14 is correct and that the water component of conduction in olivine indeed has a low activation enthalpy. Thus it is likely that a non-diffusional water mechanism (or some other mechanism) with a low activation enthalpy is required to resolve conductivity discrepancies between measured and predicted olivine.

## Conclusion

In conclusion we predict that water increases both the Mg diffusion rate of forsterite and the anisotropy significantly with these increases being over 2 and 5 orders of magnitude, respectively in the right conditions. The increase in diffusion rate is proportional to the water concentration while the increase in anisotropy does not depend on the concentration except at very low water concentrations (< ~ 1 wt. ppm). This low water concentration (< 1 wt. ppm) can be regarded as the crossover point from “dry” to “wet” diffusion laws. These increases in diffusion rate and anisotropy are large and should be visible in experiments though we are not aware of any experiments which expressly measure the anisotropy of Mg diffusion in wet forsterite.

We predict that both the magnitude of the increase in Mg diffusion rates and the exponent that governs how they change with water concentration vary strongly depending upon environmental conditions. This is because they are related to the concentration of  $(2H)_{Mg}^X$  which also has strong condition dependence. Notably increasing the pressure decreases the effect of water on diffusion as it promotes  $(4H)_{Si}^X$  over  $(2H)_{Mg}^X$ . We showed the effect of this complexity by plotting Mg diffusion in forsterite along a geotherm and find that in wet forsterite it peaks around 100 km in an oceanic geotherm with sharp decreases in diffusion rate on either side of this depth. This demonstrates that Mg diffusion rates in wet forsterite cannot be modelled with one simple parameter and that the full system of water distribution and  $(2H)_{Mg}^X$  diffusion rates need to be taken into account to model Mg diffusion. We find a good match between the calculated diffusivity of  $(2H)_{Mg}^X$  and experimental measures of hydrogen diffusivity in forsterite suggesting that H diffusion primarily operates through  $(2H)_{Mg}^X$  diffusion. This means that all the

above conclusions about the effect of water on Mg diffusion rates and anisotropy should also apply to hydrogen diffusion. Finally we consider the effect of our predictions on wet conductivity rates in olivine and find very large differences between our predicted conductivities and those observed in olivine suggesting that the effect of water on olivine conductivity is not through ionic diffusion.

**Supplementary Information** The online version contains supplementary material available at <https://doi.org/10.1007/s00269-022-01204-7>.

**Acknowledgements** Funding was provided by the National Natural Science Foundation of China (41773057, 42050410319), Science and Technology Foundation of Guizhou Province (ZK2021-205), and by the National Environment Research Council as part of the Volatiles, Geodynamics and Solid Earth Controls on the Habitable Planet research programme (NE/M000044/1). JM is highly thankful to Chinese Academy of Sciences (CAS) for PIFI.

## Declarations

**Conflict of interest** The authors declare no competing interests.

## References

- Berry AJ, O'Neill HSC, Hermann J, Scott DR (2007) The infrared signature of water associated with trivalent cations in olivine. *Earth Planet Sci Lett* 261:134–142
- Chakraborty S (2010) Diffusion in minerals and melts. In: Zhang YX, Cherniak DJ, Rosso J (eds) *Reviews in mineralogy and geochemistry*, vol 72. DeGruyter, New York
- Constable S, Shankland TJ, Duba A (1992) The electrical-conductivity of an isotropic olivine mantle. *J Geophys Res-Solid Earth* 97:3397–3404
- Costa F, Chakraborty S (2008) The effect of water on Si and O diffusion rates in olivine and implications for transport properties and processes in the upper mantle. *Phys Earth Planet Inter* 166:11–29
- Dai L, Karato S-I (2014) Influence of oxygen fugacity on the electrical conductivity of hydrous olivine: implications for the mechanism of conduction. *Phys Earth Planet Inter* 232:57–60
- Dai L, Karato S-I (2020) Electrical conductivity of ti-bearing hydrous olivine aggregates at high temperature and high pressure. *J Geophys Res-Solid Earth* 125:e2020JB020309
- Dai L, Li H, Li C, Hu H, Shan S (2010) The electrical conductivity of dry polycrystalline olivine compacts at high temperatures and pressures. *Mineral Mag* 74:849–857
- Demouchy S, Bolfan-Casanova N (2016) Distribution and transport of hydrogen in the lithospheric mantle: a review. *Lithos* 240:402–425
- Fei HZ, Koizumi S, Sakamoto N, Hashiguchi M, Yurimoto H, Marquardt K, Miyajima N, Katsura T (2018) Mg lattice diffusion in iron-free olivine and implications to conductivity anomaly in the oceanic asthenosphere. *Earth Planet Sci Lett* 484:204–212
- Fei H, Druzhbin D, Katsura T (2020) The effect of water on ionic conductivity in olivine. *J Geophys Res-Solid Earth* 125:e2019JB019313
- Gardes E, Gaillard F, Tarits P (2014) Toward a unified hydrous olivine electrical conductivity law. *Geochem Geophys Geosyst* 15:4984–5000
- Green DH, Ringwood AE (1970) Mineralogy of peridotitic compositions under upper mantle conditions. *Phys Earth Planet Inter* 3:359–371
- Han K, Guo XZ, Zhang JF, Wang XB, Clark SM (2021) Fast grain-boundary ionic conduction in multiphase aggregates as revealed by electrical conductivity measurements. *Contrib Miner Petrol* 176:1–19
- Isaak DG, Anderson OL, Goto T, Suzuki I (1989) Elasticity of single-crystal forsterite measured to 1700-K. *J Geophys Res-Solid Earth Planets* 94:5895–5906
- Jaoul O (1990) Multicomponent diffusion and creep in olivine. *J Geophys Res-Solid Earth Planets* 95:17631–17642
- Jollands MC, Hermann J, St H, O'Neill C, Spandler C, Padron-Navarta JA (2016) Diffusion of Ti and some Divalent Cations in Olivine as a Function of Temperature, Oxygen Fugacity, Chemical Potentials and Crystal Orientation. *J Petrol* 57:983–2010
- Jollands MC, Zhukova IA, O'Neill HS, Hermann J (2020) Mg diffusion in forsterite from 1250–1600 °C. *Am Miner.* <https://doi.org/10.2138/am-2020-7286>
- Jung H, Karato SI (2001) Effects of water on dynamically recrystallized grain-size of olivine. *J Struct Geol* 23:1337–1344
- Karato S-I (2013) Theory of isotope diffusion in a material with multiple species and its implications for hydrogen-enhanced electrical conductivity in olivine. *Phys Earth Planet Inter* 219:49–54
- Karato S, Jung H, Katayama I, Skemer P (2008) Geodynamic significance of seismic anisotropy of the upper mantle: new insights from laboratory studies. *Annu Rev Earth Planet Sci* 36:59–95
- Kohlstedt DL (2006) The role of water in high-temperature rock deformation. In: Keppeler H, Smyth JR (eds) *Water in nominally anhydrous minerals*. Mineralogical Soc Amer & Geochemical Soc, Chantilly
- Kohlstedt DL, Mackwell SJ (1998) Diffusion of hydrogen and intrinsic point defects in olivine. *Zeitschrift Fur Physikalische Chemie-International Journal of Research in Physical Chemistry & Chemical Physics* 207:147–162
- Kroger FA, Vink HJ (1956) Relations between the concentrations of imperfections in crystalline solids. *Solid State Physics* 3:307–435
- Kung J, Li BS, Uchida T, Wang YB, Neuville D, Liebermann RC (2004) In situ measurements of sound velocities and densities across the orthopyroxene -> high-pressure clinopyroxene transition in MgSiO<sub>3</sub> at high pressure. *Phys Earth Planet Inter* 147:27–44
- McCluskey MD, Tarun MC, Teklemichael ST (2012) Hydrogen in oxide semiconductors. *J Mater Res* 27:2190–2198
- Muir JMR, Jollands M, Zhang FW, Walker AM (2020) Explaining the dependence of M-site diffusion in forsterite on silica activity: a density functional theory approach. *Phys Chem Minerals* 47:1–16
- Muir J, Zhang F, Walker AM (2021) The mechanism of Mg diffusion in forsterite and the controls on its anisotropy. *Phys Earth Planet Inter* 321:106805
- Muir JMR, Jollands M, Zhang F, Walker AM (2022) Controls on the distribution of hydrous defects in forsterite from a thermodynamic model. *Phys Chem Minerals* <https://doi.org/10.31223/X54613>
- Novella D, Jacobsen B, Weber PK, Tyburczy JA, Ryerson FJ, du Frane WL (2017) Hydrogen self-diffusion in single crystal olivine and electrical conductivity of the Earth's mantle. *Sci Rep* 7:10
- Padron-Navarta JA, Hermann J, O'Neill HSC (2014) Site-specific hydrogen diffusion rates in forsterite. *Earth Planet Sci Lett* 392:100–112
- Schock RN, Duba AG, Shankland TJ (1989) Electrical-conduction in olivine. *J Geophys Res-Solid Earth Planets* 94:5829–5839
- Speziale S, Zha CS, Duffy TS, Hemley RJ, Mao HK (2001) Quasi-hydrostatic compression of magnesium oxide to 52 GPa: implications for the pressure-volume-temperature equation of state. *J Geophys Res-Solid Earth* 106:515–528

- Sun W, Yoshino T, Kuroda M, Sakamoto N, Yurimoto H (2019) H-D interdiffusion in single-crystal olivine: implications for electrical conductivity in the upper mantle. *J Geophys Res-Solid Earth* 124:5696–5707
- Tollan PME, Smith R, O'neill HSC, Hermann J (2017) The responses of the four main substitution mechanisms of H in olivine to H<sub>2</sub>O activity at 1050 degrees C and 3 GPa. *Progr Earth Planet Sci* 4:1–20
- Vineyard GH (1957) Frequency factors and isotope effects in solid state rate processes. *J Phys Chem Solids* 3:121–127
- Wang ZY, Hiraga T, Kohlstedt DL (2004) Effect of H<sup>+</sup> on Fe-Mg interdiffusion in olivine, (Fe, Mg)<sub>2</sub>SiO<sub>4</sub>. *Appl Phys Lett* 85:209–211
- Yoshino T, Matsuzaki T, Shatskiy A, Katsura T (2009) The effect of water on the electrical conductivity of olivine aggregates and its implications for the electrical structure of the upper mantle. *Earth Planet Sci Lett* 288:291–300
- Yoshino T, Zhang BH, Rhymer B, Zhao CC, Fei HZ (2017) Pressure dependence of electrical conductivity in forsterite. *J Geophys Res-Solid Earth* 122:158–171

**Publisher's Note** Springer Nature remains neutral with regard to jurisdictional claims in published maps and institutional affiliations.